

Jasinski Jamie Matthew (Orcid ID: 0000-0001-9969-2884)

Slavin James A. (Orcid ID: 0000-0002-9206-724X)

Raines Jim M (Orcid ID: 0000-0001-5956-9523)

DiBraccio Gina A. (Orcid ID: 0000-0002-2778-4998)

## **Mercury's solar wind interaction as characterized by magnetospheric plasma mantle observations with MESSENGER**

**Jamie M. Jasinski<sup>1</sup>, James A. Slavin<sup>1</sup>, Jim M. Raines<sup>1</sup> and Gina A. DiBraccio<sup>2</sup>**

<sup>1</sup>Climate and Space Sciences and Engineering, University of Michigan, Ann Arbor, MI, USA.

<sup>2</sup>NASA Goddard Space Flight Center, Greenbelt, MD, USA.

Corresponding author: Jamie M. Jasinski ([jjasinski@umich.edu](mailto:jjasinski@umich.edu))

### **Key Points:**

- Proton and sodium ions in Mercury's southern plasma mantle have mean number densities of  $\sim 1.5$  and  $0.004 \text{ cm}^{-3}$ , respectively
- The highest estimate of mantle proton and sodium flux supply to the plasma sheet are  $1.5 \times 10^8 \text{ cm}^{-2} \text{ s}^{-1}$  and  $0.8 \times 10^8 \text{ cm}^{-2} \text{ s}^{-1}$ , respectively.
- An average cross-electric magnetospheric potential of  $\sim 19 \text{ kV}$  is determined, which is enhanced for increased IMF strength and  $-B_z$ .

This is the author manuscript accepted for publication and has undergone full peer review but has not been through the copyediting, typesetting, pagination and proofreading process, which may lead to differences between this version and the [Version of Record](#). Please cite this article as doi: [10.1002/2017JA024594](https://doi.org/10.1002/2017JA024594)

## Abstract

We analyze 94 traversals of Mercury's southern magnetospheric plasma mantle using data from the MESSENGER spacecraft. The mean and median proton number density in the mantle are 1.5 and 1.3  $\text{cm}^{-3}$ , respectively. For sodium number density these values are 0.004 and 0.002  $\text{cm}^{-3}$ . Moderately higher densities are observed on the magnetospheric dusk side. The mantle supplies up to  $1.5 \times 10^8 \text{ cm}^{-2} \text{ s}^{-1}$  and  $0.8 \times 10^8 \text{ cm}^{-2} \text{ s}^{-1}$  of proton and sodium flux to the plasma sheet, respectively. We estimate the cross-electric magnetospheric potential from each observation and find a mean of  $\sim 19$  kV (standard deviation of 16 kV) and a median of  $\sim 13$  kV. This is an important result as it is lower than previous estimations and shows that Mercury's magnetosphere is at times not as highly driven by the solar wind as previously thought. Our values are comparable to the estimations for the ice giant planets, Uranus and Neptune, but lower than Earth. The estimated potentials do have a very large range of values (1 – 74 kV), showing that Mercury's magnetosphere is highly dynamic. A correlation of the potential is found to the interplanetary magnetic field (IMF) magnitude, supporting evidence that dayside magnetic reconnection can occur at all shear angles at Mercury. But we also see that Mercury has an Earth-like magnetospheric response, favoring  $-B_z$  IMF orientation. We find evidence that  $-B_x$  orientations in the IMF favor the southern cusp and southern mantle. This is in agreement with telescopic observations of exospheric emission, but in disagreement with modeling.

## 1 Introduction

The magnetospheric plasma mantle is located in the nightside high latitude magnetotail. The observed plasma originates from the solar wind, entering the magnetosphere at the dayside magnetopause via magnetic reconnection. Magnetic reconnection between the interplanetary magnetic field (IMF) and the dayside magnetospheric field occurs when the fields are anti-parallel. This drives the dynamics at the terrestrial magnetospheres by opening closed magnetospheric field lines on the dayside, transporting them through the lobes and closing them

on the nightside in the magnetospheric current sheet. The closed magnetic flux is then transported to the dayside magnetosphere where it can once again be opened by dayside magnetopause reconnection. This is called the Dungey cycle [Dungey, 1961]. The top half of Figure 1 shows a schematic of Mercury's magnetosphere. The Sun is to the left and the dashed lines show the bow shock ('BS') and magnetopause ('MP').

After dayside magnetic reconnection occurs, shocked solar wind plasma is able to enter a magnetosphere through the dayside high-latitude cusps, which is shaded gold in Figure 1 [e.g. Reiff et al., 1977; Lockwood and Smith, 1994; Raines et al., 2014; Jasinski et al., 2014]. However as the field line convects anti-sunward after reconnection, some of the particles that originally entered the cusp will eventually mirror and travel along the magnetic field line away from the planet. This region of the magnetosphere is the plasma mantle. At Mercury, the plasma mantle is located in the high-latitude nightside magnetosphere [DiBraccio et al., 2015a] where plasma originating from the magnetosheath flows in a direction away from the cusps (and away from the planet), down the magnetotail along field lines inside of the magnetopause (shaded red in Figure 1). The mantle is an important feature to study as the observed particles are present due to reconnection and this region can characterize a magnetosphere's interaction with the solar wind as well as being a measure of the sources and sinks of magnetospheric plasma.

The first detection of the Earth's plasma mantle was reported from the Vela satellite observations as a thick boundary layer surrounding the magnetotail where anti-sunward magnetosheath protons were observed within the nightside magnetopause [Hones et al., 1972; Sckopke et al., 1973]. The thickness of this mantle was found to be 0.5-4  $R_E$  (where  $R_E$  is the radius of the Earth), with the flow speeds positively correlated to that of the magnetosheath, and the proton number density decreasing (from  $\sim 10$  to  $0.01 \text{ cm}^{-3}$ ) with increasing distance from the magnetopause [Rosenbauer et al., 1975]. The global thickness of the plasma mantle was observed to vary with interplanetary magnetic field (IMF) orientation, with a thicker mantle present for strongly southward IMF orientations when dayside magnetopause reconnection is

enhanced [Sckopke et al., 1976]. Pilip and Morfill [1978] also showed that the mantle is a source of material for the plasma sheet as the solar wind particles are able to  $\mathbf{ExB}$  drift from the high-latitude tail toward the central plasma sheet. Ionospheric ion outflow is another source of material for the plasma sheet [e.g. Horowitz and Moore, 1997]

Magnetohydrodynamic models also describe the plasma mantle as a standing slow-mode expansion fan, whereby the plasma mantle becomes thicker with increasing distance downtail [Siscoe and Sanchez, 1987; Sanchez and Siscoe 1990]. An important resulting effect from this increase in thickness, and the key observational characteristic of the plasma mantle, is a particle velocity dispersion. The particles are flowing anti-sunward with a downtail field-aligned velocity ( $V_{\parallel}$ ). There is also a motion of the particles perpendicular to the magnetic field due to the  $\mathbf{ExB}$  drift ( $V_{\text{perp}}=V_{\text{ExB}}$ ). The combination of these two velocities, results in a motion downtail as well as towards the plasma sheet (Figure 1). This means particles with a lower  $V_{\parallel}$ , will arrive at the plasma sheet closer to the planet, whilst particles with larger  $V_{\parallel}$  travel further downtail before arriving in the plasma sheet. Therefore, an energy dispersion is observed in the plasma mantle [e.g. Scopke and Paschmann, 1978; Slavin et al., 1985] for a spacecraft travelling orthogonal to the magnetopause, where a dropout of higher energy particles is observed closer to the plasma sheet. The dispersion is highlighted by a red line labeled '2' in Figure 1a.

In order to characterize the mantle at Mercury and understand solar wind –planetary interaction, we used data from the MErcury Surface, Space ENvironment, GEochemistry and Ranging (MESSENGER) spacecraft which was in orbit around Mercury in 2011-2015. Results from the MESSENGER mission have shown that the magnetosphere of the smallest planet is very dynamic with a short Dungey-cycle-magnetospheric-convection timescale of ~3 minutes [Slavin et al., 2009; 2010], in comparison to a 1-3 hours at Earth [e.g. Siscoe et al., 1975; Huang et al., 2002; Tanskanen et al., 2009]. At the dayside, magnetic reconnection is observed to occur between the planetary field and the IMF even at small magnetic shear angles of ~30° [DiBraccio et al., 2013], in contrast to Earth where shear angles of ~90-270° are required [Burton et al.,

1975; Mozer and Retino 2007]. Flux transfer event (FTE) observations occur when reconnection occurs at multiple x-lines along the dayside magnetopause which twist the magnetic fields into a rope-like configuration [e.g. Russell and Elphic, 1978, 1979; Fu and Lee, 1985; Jasinski et al., 2016]. FTEs at Mercury are extremely common, and have been observed as “FTE showers” with separations of  $\sim 8$ s between events [Slavin et al., 2012]. At Earth, FTEs are observed to occur every  $\sim 8$  minutes [Rijnbeek et al., 1984]. Imber et al., [2014] conservatively estimated that FTEs can supply up to a third of the open magnetic flux content at the magnetosphere at Mercury, in comparison to the 2% estimated at Earth [Milan et al., 2007]. Therefore FTEs are more likely to play an important role in supplying the mantle with plasma at Mercury, as well as the plasma mantle being an important source of plasma in the Mercury’s magnetosphere. The first observation of the southern plasma mantle at Mercury was reported by *DiBraccio et al.* [2015a]. In this study, the authors presented two traversals of the mantle on the same day, where an ion energy-latitude dispersion was observed as well as frequent FTE observations in the adjacent magnetosheath. From these dispersions the cross-magnetospheric electric potentials were estimated to be  $\sim 23$  and  $\sim 29$  kV.

In this paper we present a survey of southern plasma mantle observations completed by the MESSENGER spacecraft between 2011 and 2015 in order to better understand the plasma mantle contribution to magnetospheric dynamics at Mercury and quantify its characteristics. We first describe the instrumentation, followed by the selection criteria from observations for our study and the results.

## **2 Instrumentation**

Data from the following MESSENGER instrumentation were used for this analysis: the Fast Imaging Plasma Spectrometer (FIPS) [Andrews et al., 2007] and the Magnetometer (MAG) [Anderson et al., 2007].

FIPS was a time-of-flight mass spectrometer that measured ions with an energy-per-charge range of 46 eV-13 keV/q, a mass-per-charge range of 1-60 amu/q, with a time resolution of  $\sim 8$  s. The angular resolution was  $\sim 15^\circ$ , and the effective field of view of the instrument was  $\sim 1.15\pi$  sr as  $\sim 0.25\pi$  sr was blocked by the spacecraft sunshade. MAG was a fluxgate magnetometer mounted on a 3.6 m long boom, with a resolution of 0.047 nT and a maximum time resolution of 20 vectors  $\text{s}^{-1}$ . The magnetic field measurements are presented in Mercury Solar Orbital (MSO) coordinates, where X is in the planet-Sun direction, -Y points towards planetary orbital velocity vector direction and Z completes the right hand set and points northward.

### 3 Observations

#### 3.1. Overview for a typical MESSENGER orbit

For trajectories close to the noon-midnight meridian, the MESSENGER spacecraft crossed the nightside southern magnetopause. This means plasma mantle detections can occur between the tail lobe (low plasma density, high magnetic field strength) and the magnetosheath (high plasma density, lower magnetic field strength), both adjacent to the mantle. Depending on the direction of the trajectory (planetward or anti-planetward) the observations of the region of interest are in the chronological order of magnetosheath  $\rightarrow$  mantle  $\rightarrow$  lobe for a planetward trajectory and the opposite for an outward trajectory.

An example of this typical trajectory and the corresponding MESSENGER observations are displayed in Figure 1. The data for the trajectory (data panel a) start and end at the arrowheads (left and right, respectively, clockwise). The observations begin in the solar wind, where low ion fluxes are measured near  $\sim 1$  keV. The spacecraft then crossed the bow shock (BS) and entered the magnetosheath (M'sheath) at  $\sim 22:13$  UT, where the magnitude of the magnetic field increased from  $\sim 25$  to  $\sim 80$  nT, and FIPS observed the dense, shocked solar wind plasma (a). At  $\sim 22:30$  UT the spacecraft crossed the magnetopause (MP), and entered the magnetosphere where tenuous energetic plasma was observed, followed by the cusp (gold) where magnetosheath

plasma with an energy-latitude dispersion (higher energies observed at lower latitudes - underlined in red and labeled '1') was observed at ~23:37 UT. The spacecraft then observed the northern tail lobe before crossing the plasma sheet (~23:00 UT) where energetic plasma was observed and the  $B_x$  component (blue in panel b) of the magnetic field was equal to ~0 nT. Before entering the plasma mantle the southern lobe was observed (as indicated by the  $-B_x$  orientation) where no plasma is detected within the threshold of FIPS. Whilst in the mantle, higher energies were observed closer to the magnetopause due to the effect of  $V_{\text{ExB}}$  as described above (this dispersion is underlined in red and labeled '2'). The spacecraft crossed the magnetopause once again where it observed the magnetosheath.

Large fluctuations in the magnetic field data can be seen at the magnetopause (the magnetopause is marked by the middle and right vertical dashed lines), as well as in the plasma sheet. These are largely due to the presence of flux ropes, with flux transfer events being observed at the magnetopause and plasmoids in the plasma sheet [e.g. Slavin et al., 2012; Imber et al., 2014; DiBraccio et al., 2015b], as well as dipolarisation fronts in the plasma sheet [Sundberg et al., 2012; Sun et al., 2016].

The  $0.196 R_M$  northward offset of Mercury's dipole [Anderson et al., 2011] results in different features for the plasma in the northern and southern parts of the magnetosphere, resulting in a plasma asymmetry in the nightside [Korth et al., 2014]. The asymmetry affects the plasma in the cusps and therefore the resulting plasma observed in the northern or southern mantle. Due to the trajectory of MESSENGER we only survey observations from the southern mantle. We do not expect the northern mantle to be similar to the observed southern mantle due to the above mentioned asymmetry.

### **3.2 Data selection method**

The plasma mantle observations were identified by the ion energy dispersion observed in the FIPS data similarly to the first plasma mantle observations at Mercury [DiBraccio et al., 2015a].

MESSENGER observations of two example mantle traversals can be seen in Figures 2 and 3, for an inbound and outbound trajectory, respectively. Figure 2 shows a scenario where the spacecraft passed from the southern lobe into the plasma mantle (bounded by the two vertical lines) and out into the magnetosheath, while in Figure 3, MESSENGER crossed the boundaries in the reverse order. Figures 2 and 3 are in the same format, with proton flux, proton number density and sodium counts all from FIPS shown in panels a-c, respectively. Proton number density was estimated using a forward modeling technique, a method used in previous papers [Raines et al., 2011; Gershmann et al., 2013] the values of which have been delivered to the Planetary Data System [Ho et al., 2016]. This is followed by magnetometer measurements, including the three components of the magnetic field in MSO coordinates and magnitude shown in panels d and e, respectively.

The inner boundary of the mantle (adjacent to the southern lobe, where no plasma is observed by FIPS) was determined by the inner most signal-to-noise ratio (SNR)  $\geq 2$  in the FIPS measured proton counts. This can be seen in Figure 2a and 3a, where the highest energy bin with an SNR  $\geq 2$  for each FIPS accumulation is marked by a green dot. The inner boundary of the mantle, adjacent to the tail lobe, is marked by the first (second) vertical dashed line in Figure 2a (3a) where the SNR meets this selection threshold. The SNR threshold also makes the ion energy dispersion more clear (highlighted by the red line).

The outer boundary of the mantle, adjacent to the magnetosheath, was selected on the basis of the magnetic field variation ( $\Delta B$ ) observed by MAG. This is due to the magnetic field varying significantly more in the magnetosheath adjacent to the mantle than within the magnetosphere. The magnetic field variation was calculated using:

$$\Delta B_i = \sqrt{\frac{(b_i - B_{ave_i})^2}{20}} \quad (1)$$



where  $B_{ave_i}$  is a 21 point running average (i.e. ~1s average) centered at data point  $b_i$ . A smoothing average filter was applied to  $\Delta B_i$  by calculating a thousand-point average. The outer boundary of the mantle was selected when the magnetic field variability  $\Delta B_i$  was drastically greater than its thousand point average (defined as when  $\Delta B_i > 3.7 \Delta B_{1000\text{-point-average}}$ ). Initially, the outer boundary selection process was focused on finding where the magnetic field rotated as the spacecraft crossed the magnetopause boundary (as can be seen at ~18:10 UT in Figure 2d-e). However not all the magnetopause crossings present a field rotation, and therefore, we chose to use the magnetic field variability instead as it is more reliable.

A total of 94 mantle crossings were identified, including the two observations reported by DiBraccio et al. (2015a). As can be seen in Figure 4, plasma mantle observations occurred in the southern nightside region of the magnetosphere. The observations are in the southern hemisphere only because of the orbital configuration of MESSENGER which never had the opportunity to explore the northern mantle region. The location of the observations can be seen in Figure 4, shown in aberrated Magnetospheric-Solar-Orbital (MSO) coordinates. The coordinates are aberrated to account for the high orbital velocity of the planet (39-59 km/s), which results in the effective solar wind arrival vector being offset by ~7 deg from the  $X_{MSO}$  direction. The orbital velocity varies over the Mercury's year due to its highly eccentric orbit. The degree of aberration is also dependent on the solar wind velocity. Here we use the aberration determined by Boardsen et al., (2010), which calculated the aberration angle for each day by assuming a 410 km/s solar wind speed.

Figure 4 also shows the spatial distribution of the average proton (panels a-c) and sodium (panels d-e) number densities in the plasma mantle in the three different planes. The density in this figure is the average measured number density of every measurement FIPS made in Mercury's plasma mantle during a given traversal. To ensure that the results were not affected by the FIPS field of view (FOV), we checked for density variations in the different instrument look directions. During the mantle observations, the FIPS FOV was ~42-270° from the Y-MSO

direction in the Y-Z MSO plane ( $0^\circ$  and  $90^\circ$  being in the Y and Z MSO directions, respectively). The density trends discussed below were the same for FOV bins of  $45\text{-}135^\circ$  and  $135\text{-}225^\circ$ , which means that they are not a result of instrument effects but are physical results. It can be generally seen that the mantle is denser closer to the magnetopause. This can be seen more clearly for a specific mantle crossing, in a density line plot shown in Figure 2b. As MESSENGER approaches the magnetopause, the plasma density increases gradually. Figures 4b and c also show a modest increase in density of the plasma mantle towards dusk. This is due to the centrifugal drift that the ions experience close to the planet due to the curvature of the magnetic field [e.g. Delcourt et al., 2003]. The resulting drift is in the duskward direction, which explains the higher densities in the plasma mantle in the dusk sector. Panels d-f are in the same format as a-c but are shown for sodium number density. The sodium observation follows a similar trend as the protons, with slightly higher densities in the dusk sector. However it does not appear that the sodium is denser nearer the magnetopause.

### 3.3 IMF Correlation

The plasma mantle observations were also compared to the IMF conditions. IMF observations to the nearest bow shock crossing were averaged over a two-minute interval. We also calculated the average over a 20 minute interval to provide an estimate of the variability of the IMF. Figures 5a and b show histograms of the average plasma mantle proton and sodium number density, respectively, organized by IMF orientation in the north-south direction,  $B_Z$ . From these figure we can see that the observation of the plasma mantle is more likely to occur for  $-B_Z$  conditions. The plasma mantle is also more likely to be denser during  $-B_Z$ . Like at Earth, these observations are due to  $-B_Z$  resulting in higher reconnection rates at the dayside subsolar magnetopause, which are more likely to inject larger numbers of plasma into the magnetosphere which are eventually observed in the plasma mantle.

Figure 5c shows the observed sodium ion densities in comparison to proton density measurements (both observed in the mantle). Sodium observations are common at Mercury's magnetosphere and are present due to sputtering at the planet's surface [e.g. Raines et al., 2014]. For times when FIPS observes sodium, the sodium density has a strong dependence on the proton density (i.e. we see higher sodium with higher proton densities). However we do not always observe sodium in the plasma mantle. We also did not observe a dependence of the sodium density on the IMF magnitude.

### 3.4 Estimating the electric potential and plasma flux

#### 3.4.1 Calculation of the magnetospheric cross-electric potential

From the plasma mantle observations (FIPS and MAG) we are able to estimate the electric field  $\mathbf{E}$ , using  $\mathbf{E} = -\mathbf{V}_{\mathbf{E} \times \mathbf{B}} \times \mathbf{B}$ , where  $\mathbf{V}_{\mathbf{E} \times \mathbf{B}}$  is the drift velocity and  $\mathbf{B}$  is the magnetic field. We then use these values of  $\mathbf{E}$  to estimate the magnetospheric cross-electric potential ( $\Phi$ ), as described by *DiBraccio et al.*, [2015a]. Considering the high-latitude trajectory of MESSENGER we assume that the spacecraft was travelling orthogonal to the magnetopause. Therefore, we estimate  $\mathbf{V}_{\mathbf{E} \times \mathbf{B}}$  by assuming  $\mathbf{V}_{\mathbf{E} \times \mathbf{B}} \sim V\theta$ , where  $\theta$  is the dispersion wedge angle calculated geometrically from  $L$  and  $d$  which are shown in Figure 1.  $L$  is the distance from the day-night terminator in the  $X_{\text{MSO}}$  direction and  $d$  is the thickness of the mantle in the  $Z_{\text{MSO}}$  direction. These are calculated using the position of the spacecraft in the magnetosphere and its distance from the magnetopause.  $V$  is the plasma velocity observed by the FIPS instrument. This is calculated from a weighted mean of proton energy distributions based on the flux measurements. We then calculate  $E$  using  $\mathbf{V}_{\mathbf{E} \times \mathbf{B}}$  and the average observed magnetic field  $B$  by MAG. The cross-electric potential is determined by  $\Phi = Ed_{\text{tail}}$ , where  $d_{\text{tail}}$  is the magnetotail width and is taken to be  $\sim 5 R_{\text{M}}$  consistent with the average values estimated previously [*Slavin*, 2003; *Winslow et al.*, 2013; *Sun et al.*, 2015]. For each mantle crossing, this method is completed for every FIPS measurement over a single traversal

and then averaged to produce a potential estimation for every event. For more details about this method please refer to DiBraccio et al., [2015a].

There are uncertainties associated with our calculations. Firstly, the calculation is dependent on our selection criteria, specifically the location of the outer boundary of the plasma mantle (the magnetopause) from the observed magnetic variation,  $\Delta B_i$ . DiBraccio et al., [2015a] visually identified the magnetopause based on magnetic field rotations. For this study, however, there is not always a clear rotation at the boundary and our approach of utilizing magnetic field variations is more appropriate for a larger dataset. It should be noted that this method is more likely to select the most inner boundary of the magnetopause; therefore, our electric potential calculations are likely lower limits. In comparison to the DiBraccio et al., [2015a] calculations for the two mantle events observed on November 10<sup>th</sup> 2012 (~23 and ~29 kV), we calculated potentials of ~21 and ~23 kV, respectively. This corresponds to a difference of ~9 and ~20% to DiBraccio et al., [2015a] calculations. Using their selection criteria for the example shown in Figure 2, the magnetopause would be selected at the field rotation observed at 18:03:45 UT (one time tick to the right of the second vertical dashed line in Figure 2). The difference in the calculated potential from their method in comparison to ours is the same to zero decimals. Similarly we calculated the potentials for the event which shows the largest time difference between the field rotation and our selection time. For the September 28<sup>th</sup> 2011 mantle event the calculated potentials using the DiBraccio et al., [2015a] method (of magnetopause identification) and ours is ~23 kV and ~17 kV, respectively. This represents a difference of ~26%. Therefore we estimate that our calculations may underestimate the potential by an upper limit of ~25% for some (but not all) events. To account for this underestimation we present our estimated potentials as 125% of the values calculated from this method.

Other uncertainties manifest themselves from the method we have used here. The width of the magnetotail ( $d_{\text{tail}}$ ) is the average value estimated by Winslow et al., [2013] which may vary by up to  $2 R_M$ . The value of  $L$  may also vary depending on where the solar wind particles were injected

in the cusp [Raines *et al.*, 2014] and where they mirror along their trajectory. Therefore our  $L$  estimate is most likely a lower value, but it would not increase by more than  $\sim 0.5 R_M$ , since the dayside subsolar magnetopause is located on average less than  $0.5 R_M$  from the surface of Mercury [Winslow *et al.*, 2013]. The FIPS instrument does not sample the complete plasma velocity distribution due to its field of view constrictions, and therefore the speed may be higher than the ones calculated here [Gershman *et al.*, 2012].

A histogram of the estimated cross-magnetospheric electric potential for each plasma mantle event (corrected for the underestimation as discussed above) is shown in Figure 5d. We estimate a wide range of potentials at Mercury (1-74 kV). The average is  $\sim 19$  kV and the median  $\sim 13$  kV. These values are lower than previous estimates [e.g. Imber *et al.*, 2014; DiBraccio *et al.*, 2015a]. However, our study includes all MESSENGER observations and does not focus on large amplitude events (such as the large FTEs observed by Imber *et al.*, 2014; and the large mantle dispersion observed by DiBraccio *et al.*, 2015a). Therefore our study includes quiet magnetospheric conditions as well as the extreme events. We do observe a large variety of potentials which shows that Mercury's magnetosphere is very dynamic and active.

### **3.4.2 Estimating the plasma flux supply to the plasma sheet**

Using the estimated ExB drift velocity from the previous section, we have also estimated the subsequent particle flux that the plasma mantle supplies to the nightside plasma sheet located in the magnetotail. We assumed the protons had pitch angles of  $45^\circ$  (from FIPS measurements the observed pitch angles are largely  $45-90^\circ$ ), with the magnetic field directed anti-sunward. We estimated the particle energies that would be lost downtail (past the nightside tail reconnection location) based on their observed energies (and therefore velocities) in comparison to the estimated  $V_{\text{EXB}}$ . Here, we assume that the nightside tail reconnection location is at  $\sim 3 R_M$  [Poh *et al.*, 2017]. We estimated the integrated flux in the mantle using this energy cutoff to estimate the proton flux supply to the plasma sheet. This was done for every FIPS accumulation and then

averaged for each mantle event (similarly to the cross-magnetospheric electric potential discussed above).

Due to the locations of our plasma mantle observations occurring at large downtail distances (up to  $-4 R_M$  in the  $X'$ -MSO direction), most of the observed protons during our crossings are lost downtail. Only 7 of the 94 mantle crossings present plasma that enters the plasma sheet planetward of the reconnection location. If we assume field-aligned pitch angles of  $0^\circ$ , this number falls to 5. Assuming the particles have a close-to-perpendicular pitch angles ( $80^\circ$ ), 38 of the mantle events measured protons that would populate the plasma sheet. The largest estimated proton flux to the plasma sheet from a single mantle event is  $1.5 \times 10^8 \text{ cm}^{-2} \text{ s}^{-1}$ . For the calculations assuming the proton pitch angle is  $80^\circ$ , the average plasma flux to the plasma sheet from our events (for when the mantle is able to supply the plasma sheet) was  $3.6 \times 10^7 \text{ cm}^{-2} \text{ s}^{-1}$ . Using the same method, we estimated the flux for sodium entering the plasma sheet and found the largest to be  $0.8 \times 10^8 \text{ cm}^{-2} \text{ s}^{-1}$  and an average of  $0.6 \times 10^8 \text{ cm}^{-2} \text{ s}^{-1}$ . The average value is half that for the protons. Even though the observed fluxes of protons are much greater in the mantle than the sodium, due to the higher mass of sodium the parallel velocity is lower; therefore less sodium is lost downtail in comparison to protons, and a larger fraction of the sodium enters the plasma sheet.

### **3.5 When do we not observe the mantle?**

We have also investigated periods in MESSENGER's orbit when the spacecraft did not observe the plasma mantle. We investigated magnetopause crossings in the nightside of the magnetosphere within  $\pm 1 R_M$  in aberrated  $Y'_{\text{MSO}}$  direction. These trajectories can be seen in Figure 6a and b (this is MESSENGER's trajectory for five minutes equatorward of the magnetopause crossing). For consistency with plasma mantle observations, we also removed any trajectories that did not have the same FOV for FIPS as the mantle crossings. The mantle was

observed with FOV angles greater than  $45^\circ$  away from the  $+Y_{\text{MSO}}$  direction. This removes  $\sim 5\%$  of the remaining trajectories. With these criteria there were 957 times when the mantle was not observed. We obtained the IMF conditions for these events using the same method that we used for the plasma mantle events (discussed above).

Figure 6c-f compares the IMF conditions when the plasma mantle was observed (red) and not observed (blue). Figure 6c shows the comparison of the IMF magnitude. For both, the distribution peaks at the 25 nT centered bin. However, we can see that the mantle is much more likely to be seen for IMF magnitudes at and below this value. We will show that the magnetospheric potential increases for larger IMF magnitudes (shown below in Section 3.6). However, this figure shows that we are less likely to observe the mantle for the much higher magnitudes. This is because higher field strengths at the dayside magnetopause reconnection location will produce higher parallel electric fields [Li et al., 2017] which are more likely to create particle distributions with more field-aligned pitch angle velocities [Egedal et al., 2012]. This results in less particles mirroring, and instead more particles are lost to the surface. This means that a plasma mantle is less likely to be formed.

Figure 6d compares the  $B_z$  orientation of the IMF to when we see and do not see the plasma mantle. From this histogram, we conclude that the mantle is much more likely to be observed for a southward ( $-B_z$ ) pointing IMF than a northward one.

### 3.5.2 Dependence on the IMF $B_x$ component

Figures 6e and 6f show the mantle observation with the  $B_x$  IMF component for southward ( $-B_z$ ) and northward ( $+B_z$ ) directed IMF, respectively. We separated the  $B_x$  observations into northward and southward  $B_z$  to try and eliminate the possibility of mistaking any radial dependency on the north-south component of the IMF. We can see that for both cases we are more likely to observe (in the southern magnetosphere for our trajectory) plasma mantle for  $-B_x$ , than for  $+B_x$ . From the distribution and the comparison of the means and medians between when

MESSENGER observes the mantle and when it does not, it appears that the  $B_X$  component is more likely to have a stronger effect when  $B_Z$  is northward, and therefore reconnection is occurring at the high latitude magnetopause.

Our  $B_X$  correlation results are inconsistent with models [Sarantos *et al.*, 2001; Massetti *et al.*, 2007], where the results indicate the opposite correlation of  $+B_X$  conditions in IMF favouring the southern cusp (we observe  $-B_X$  conditions favouring the southern mantle and therefore the southern cusp). However, observations of exospheric sodium emission and their correlation to the IMF (specifically  $B_X$ ) agree with our results [Mangano *et al.*, 2015; Massetti *et al.*, 2017]. Mangano *et al.* [2015] had the strongest correlation (78%) to their observation of enhanced emission in the northern exosphere was with  $+B_X$ , and also more frequent (73%) when the IMF had large magnitudes ( $>25$  nT). Massetti *et al.*, [2017] also mentioned that they observe a  $B_X$  correlation that is opposite to the previous modeling work, however do not discuss this further. The modeling does not explicitly explore varying  $B_X$  with consistent  $B_Y$  and  $B_Z$  values, and largely just explore the behavior with regards to typical parker spiral conditions. We therefore suggest that previous modeling studies do not agree with the growing body of observational results, which may be due to this lack of consistency.

### 3.6 Other Solar wind correlations

Comparisons of the solar wind to the estimated cross-electric magnetospheric potential are shown in Figure 7. The error bars are the representations of the variability of the IMF observed over the 20 minute interval in comparison to the 2 minute average (discussed above). Shown in grey are box and whisker plots to represent the interquartile range and the median (see caption for details).



The strongest correlation of the estimated potential was to the observed magnetic field magnitude  $|B_{(\text{IMF})}|$  (Figure 7a). We used Deming regression to fit for a line of best fit (red line). Higher values of the  $|B_{(\text{IMF})}|$  would increase the field strength in the magnetosheath, and therefore would produce a lower plasma  $\beta$  (thermal to magnetic pressure ratio) in the magnetosheath. A lower plasma  $\beta$  has been shown to make reconnection much more likely at the magnetopause [Swisdak et al., 2003] and has been observed at Mercury [DiBraccio et al., 2013].

A weak correlation was observed with both the  $B_{\text{IMF}}$  and the  $B_{Z(\text{IMF})}$  orientation (Figure 7b), with the potential on a colored scale. We see that the low potential estimates (bluer colors) are clustered at lower  $B_{\text{IMF}}$  values and  $B_Z$  values closer to 0 nT. For larger  $B_{\text{IMF}}$  ( $> 35$  nT) and more negative  $B_Z$  ( $< 10$  nT) the potential is generally higher (red colors). We can see that the potential is therefore dependent on both higher IMF magnitudes and more southward orientated IMF.

Figure 8a shows the dependence of the observed magnetic field strength in the mantle to the IMF field magnitude. As the latter increases so does the former. As the reconnection rate increases due to a higher IMF magnitude more magnetic flux is transported from the dayside into the nightside which increases the observed magnitude in the plasma mantle.

Figure 8b shows a histogram of the IMF  $B_Y$  component strength divided into three groups: blue for plasma mantle observations in the noon sector (23:00 to 01:00 local time in aberrated coordinates), red for observations at dawn (after 01:00 LT) and green for observations at dusk (before 23:00 LT). The bins for noon observations peak near 0 nT, whilst the dawn and dusk bins peak for  $-B_Y$  and  $+B_Y$  IMF fields. Therefore, we can see a strong dependence of the location of the plasma mantle observation on the orientation of the IMF  $B_Y$  component. If the IMF has a large component in the  $+B_Y$  direction, then the reconnected field line has a convection direction towards dusk, resulting in the plasma mantle to be more likely to be observed there. This effect has been previously observed at Earth [e.g. Gosling et al., 1990; Cowley et al., 1991; Pitout et al., 2006].

### **3.7 Online supporting material**

In the online supporting material we provide a list of mantle event times and we present the event described in the error discussion of section 3.3 (September 28<sup>th</sup> 2011).

## **4 Discussion and Conclusions**

### **4.1 Discussion**

We have presented a survey of southern plasma mantle observations at Mercury's magnetosphere using data from the ion and magnetic field measurement taken by the FIPS and magnetometer instruments, respectively. There were 94 mantle crossings in the southern hemisphere analyzed in this study. The trajectory of the spacecraft is such that only the southern mantle is observed on consequent MESSENGER orbits. The plasma in the mantle forms as a consequence of magnetic reconnection on the dayside magnetopause that injects magnetosheath plasma into the magnetosphere, that then mirrors in the cusp and is travelling anti-sunward in the nightside tail. The average mantle proton and sodium number densities were found to be 1.5 and 0.004 cm<sup>-3</sup>, respectively. Due to the northward offset of Mercury's magnetospheric dipole [Anderson et al., 2011], north-south asymmetries have been observed in the magnetospheric plasma measurements [Korth et al., 2014]. We do not expect the southern plasma mantle characteristics presented here to represent the northern mantle due to the above mentioned asymmetry.

We studied the IMF conditions for which these mantle observations took place in, by averaging the IMF outside the bow shock for two minutes (and 20 minutes to account for any variability). We also compared these observations to times when MESSENGER did not observe the mantle but could have (by location and field of view of the FIPS instrument). There were 957 orbits where one would expect to observe the plasma mantle in the MESSENGER data. This demonstrates that the plasma mantle is not a permanent feature of Mercury's magnetosphere. If

we assume that reconnection at Mercury's dayside magnetopause is occurring near continuously, then this means that most of the particles injected into the cusp are lost to the planet (and do not mirror to form the plasma mantle). Superposed cusp ion observation analysis shows that ions are mainly observed to be flowing towards the planet with pitch angles of  $0-90^\circ$  measured in the northern cusp [Poh et al., 2016]. These observations took place close to the mirror point, so we assume that most of these particles did not mirror, and would not be able to form the mantle, supporting our idea that the mantle is not a permanent feature of Mercury's magnetosphere. However there are limitations to this conclusion. The supporting work only superposed 16 cusp events [Poh et al., 2016]. Although this gives a good presentation of the cusp, the number of events used is not large enough to give a more statistical idea of Mercury's cusp ions. Also, not observing the plasma mantle with MESSENGER does not mean that the mantle is not always there, but could mean that the spacecraft did not cross at the correct local time, since the  $B_Y$  component of the IMF has a moderate effect on the mantles location. However, even with these limitations, the fact that the mantle is observed so little of the time ( $<10\%$ ), we would not expect MESSENGER to "miss" the mantle 90% of the time. Therefore, we believe that our conclusion is correct and the mantle is not a permanent feature of the nightside magnetosphere.

Comparing to orbits when MESSENGER did not observe the mantle we see that the mantle is more likely to be seen at IMF magnitudes less than  $\sim 30$  nT. We attribute this to higher IMF magnitudes producing more intense reconnection at the dayside magnetopause due to the higher parallel electric fields, which will more likely inject particles with field-aligned pitch angles, that will not mirror and therefore not produce an observable mantle [Egedal et al., 2012; Li et al., 2017].

The plasma mantle is observed for a variety of IMF orientation, which supports previous work [DiBraccio et al., 2013; Slavin et al., 2014], that reconnection at Mercury can occur for low shear angles. However, our results also show that reconnection still favours southward IMF orientations, with more plasma mantle events observed for  $-B_Z$  IMF. This shows that Mercury

does have an Earth-like response with a dependence on the  $B_Z$  orientation. We also find that  $-B_X$  IMF conditions favour the southern mantle and therefore southern cusp. This agrees with previous results using remote sodium exospheric emission observations [Mangano *et al.*, 2015; Massetti *et al.*, 2017] but disagrees with previous modeling investigating this correlation [Sarantos *et al.*, 2001; Massetti *et al.*, 2007]. We suggest that previous modeling results do not agree with the growing body of observational results because they do not explicitly focus their investigation into exploring this effect, and therefore lack consistency between model runs. This  $B_X$  effect should however be investigated further.

The plasma mantle observations exhibit an ion energy dispersion. This is evident due to the trajectory of the spacecraft which is near orthogonal to the magnetopause. The tailward traveling ions experience an ExB drift towards the plasma sheet. Ions with higher energies have a larger parallel velocity and therefore, their tailward motion is less affected by the ExB drift in comparison to lower-energy ions. This means that higher energy ions are observed nearer the magnetopause. Using this observed phenomenon, we calculate the ions ExB velocity to estimate the electric field and subsequently the cross-electric magnetospheric potential,  $\Phi$ .

$\Phi$  is an important value to estimate as it is a measurement used to characterize the input of solar wind energy into a planet's magnetosphere. It is therefore useful in understanding a planet's coupling to the Sun. For Mercury, this value has been estimated in previous work, using different methods. Slavin *et al.*, [2009] reported a value of  $\sim 30$  kV during the second Mercury flyby by MESSENGER. Imber *et al.*, [2014] used the flux content found in flux transfer events observed at Mercury to estimate a potential of  $\sim 25$  kV, and DiBraccio *et al.*, [2013] found an average of  $\sim 29$  kV from dayside magnetopause crossings. Analysing two plasma mantle case studies, DiBraccio *et al.*, [2015a] estimated values of  $\sim 23$  and  $\sim 29$  kV.

We find a wide spread of calculated potentials (1-74 kV),  $\sim 66\%$  of the observations are below 20 kV and  $\sim 80\%$  are below 30 kV (see Figure 5d). The average is found to be  $\sim 19$  kV and the

median  $\sim 13$  kV. Therefore, our results show that the potential is lower at Mercury than previously thought. However, this is not completely surprising considering that previous estimates focus on observations of large events, such as the FTEs observed by *Imber et al.*, [2014] and one of the clearest plasma mantle crossings analysed by *DiBraccio et al.*, [2015a]. These studies are more likely to omit events when Mercury's magnetosphere is less dynamic and produces quieter, less intense observations. Our study focuses on a larger number of events, is the first of its kind, and therefore is a more accurate representation of Mercury's magnetosphere. The wide spread of estimated cross-magnetospheric potentials reveals how dynamic Mercury's magnetosphere is, and how much the solar wind interaction can vary.

The strongest correlation we found between the estimated potential and the IMF, was the observed magnetic field magnitude of the interplanetary magnetic field (see Figure 7a). Stronger IMF magnitudes led to higher cross-magnetospheric potentials. However, we did not find as strong a correlation between the north-south ( $B_z$ ) component of the IMF and the potential as with the magnitude. We do however observe higher potentials when both the magnitude and  $-B_z$  are large (Figure 7b). These results support previous observations [DiBraccio et al., 2013] that reconnection at Mercury can occur for a variety of shear angles, unlike at Earth or the outer planets. However, three-quarters of our observations do occur with shear angles greater than  $90^\circ$ . This shows that although reconnection can occur at various shear angles at Mercury, Mercury is still very similar to other planets where reconnection is most likely to occur with higher rates when the IMF and magnetospheric field have a high shear angle like at Earth and the outer planets.

The calculated potentials are lower than the upper limit at Earth,  $\sim 200$  kV [*Kivelson and Ridley*, 2008], and the reconnection voltages at the outer planets, Uranus and Neptune, which have been estimated to be  $\sim 40$  and  $\sim 35$  kV [*Masters*, 2014, 2015]. These however, are upper values that might not be observed due to ionospheric saturation effects. The cross-electric magnetospheric potential is affected by the ionospheric conductivity, which when high enough, affects the

currents closing in the polar cap that then limit reconnection by affecting the magnetic field at the magnetopause [e.g. *Rassbach et al.*, 1974; *Hill et al.*, 1976], so that  $\Phi \leq 2/3 \Phi_{\text{SW}}$  [*Slavin*, 2004], for planets with a significant atmosphere. However, for Mercury this is closer to  $\Phi \sim \Phi_{\text{SW}}$  due to the low conductivity of its ionosphere. Therefore, large values at Earth (150-200 kV) are rarely seen, with values closer to 50-100 kV considered more typical [e.g. *Siscoe et al.*, 2002a, 2002b]. Consequently, the potentials calculated in this study are comparable or larger than those at Uranus and Neptune, and usually lower than the values for Earth. The average of ~19 kV is also remarkably close to ~17 kV predicted by *Hill et al.*, [1976].

Even after the end of this mission, the MESSENGER spacecraft is still providing us insight into Mercury's highly dynamic and small magnetosphere. We have found that although Mercury's magnetosphere is the most highly driven by its interaction with the solar wind in comparison to other planets in the solar system, at times it is not as highly driven by the solar wind as previously thought. This is mainly due to our study being statistical in nature, whilst previous reports have focused on large events. However, further work is required to elucidate the nature of this interaction, specifically the exact role of flux transfer events in a full comprehensive statistical survey.

## 4.2 Conclusions

We have presented and analysed 94 observations of the southern plasma mantle, and 957 events when MESSENGER did not observe a plasma mantle in the south (and could have done with FIPS). From the plasma mantle observations we estimated the cross-electric magnetospheric potential. We have learnt that: 1) For the southern plasma mantle the mean and median proton number density is 1.5 and 1.3  $\text{cm}^{-3}$  respectively, and for sodium number density these values are 0.004 and 0.002  $\text{cm}^{-3}$ . 2) The highest estimate of proton and sodium flux contribution of the mantle to the plasma sheet are  $1.5 \times 10^8 \text{cm}^{-2} \text{s}^{-1}$  and  $0.8 \times 10^8 \text{cm}^{-2} \text{s}^{-1}$ , respectively. 3) The formation of the plasma mantle is strongly dependent on the upstream IMF magnitude. The

potential increases for larger IMF magnitudes, however much higher magnitudes than ~30 kV are less likely to form a plasma mantle as the particles are less likely to mirror on the dayside. 4) Even though reconnection and particle injection can occur for all shear angles at Mercury, there is however still a strong Earth-like preference for reconnection to occur for southward IMF orientations. 5) The southern mantle and therefore the southern cusp is more likely to be observed with antisunward ( $-B_X$ ) orientations. 6) The orientation of the IMF in the  $B_Y$  dictates whether the mantle is observed more duskward (for  $+B_Y$ ) or more dawnward (for  $-B_Y$ ) of the noon-midnight meridian. 7) the cross-electric potential is often lower than previous studies reported, which shows that at times Mercury's magnetosphere can be less dynamic than previously thought.

### **Acknowledgments and Data**

This research was supported by the following grants: NASA's Discovery Data Analysis (NNX15AK88G), STROFIO Investigation Science Support from Southwest Research Institute (E99061MO), Living With a Star (NNX16AJ67G), NASA grant 14-DDAP14\_2-0006 and NASA DDAP grant NNX16AJ05G. All the data used in this study can be found at NASA's Planetary Data System (<https://pds.jpl.nasa.gov>).

### **References**

- Anderson, B.J. et al. *Space Sci Rev* (2007) 131: 417. doi:10.1007/s11214-007-9246-7
- Anderson, B. J., C. L. Johnson, H. Korth, M. E. Purucker, R. M. Winslow, J. A. Slavin, S. C. Solomon, R. L. McNutt Jr., J. M. Raines, and T. H. Zurbuchen (2011), The global magnetic field of Mercury from MESSENGER orbital observations, *Science*, 333, 1859–1862, doi: 10.1126/science.1211001.
- Andrews, G et al. *Space Sci Rev* (2007) 131: 523. doi:10.1007/s11214-007-9272-5
- Boardsen, S. A., T. Sundberg, J. A. Slavin, B. J. Anderson, H. Korth, S. C. Solomon, and L. G. Blomberg (2010), Observations of Kelvin-Helmholtz waves along the dusk-side boundary of Mercury's magnetosphere during MESSENGER's third flyby, *Geophys. Res. Lett.*, 37, L12101, doi:10.1029/2010GL043606.
- Burton, R. K., R. L. McPherron, and C. T. Russell (1975), The terrestrial magnetosphere - A

- half-wave rectifier of the interplanetary electric field, *Science*, 189, 717, doi:10.1126/science.189.4204.717.
- Collier, M. R., R.P. Lepping, Jovian magnetopause breathing, *Planetary and Space Science*, Volume 44, Issue 3, 1996, Pages 187-197, ISSN 0032-0633, [http://dx.doi.org/10.1016/0032-0633\(95\)00117-4](http://dx.doi.org/10.1016/0032-0633(95)00117-4).
- Cowley, S. W. H., J. P. Morelli, and M. Lockwood (1991), Dependence of convective flows and particle precipitation in the high-latitude dayside ionosphere on the X and Y components of the interplanetary magnetic field, *J. Geophys. Res.*, 96(A4), 5557–5564, doi:10.1029/90JA02063.
- Delcourt, D. C., Grimald, S., Leblanc, F., Berthelier, J.-J., Millilo, A., Mura, A., Orsini, S., and Moore, T. E.: A quantitative model of the planetary Na<sup>+</sup> contribution to Mercury's magnetosphere, *Ann. Geophys.*, 21, 1723-1736, <https://doi.org/10.5194/angeo-21-1723-2003>, 2003.
- DiBraccio, G. A., J. A. Slavin, S. A. Boardsen, B. J. Anderson, H. Korth, T. H. Zurbuchen, J. M. Raines, D. N. Baker, R. L. McNutt Jr., and S. C. Solomon (2013), MESSENGER observations of magnetopause structure and dynamics at Mercury, *J. Geophys. Res. Space Physics*, 118, 997–1008, doi:10.1002/jgra.50123.
- DiBraccio, G. A., J. A. Slavin, J. M. Raines, D. J. Gershman, P. J. Tracy, S. A. Boardsen, T. H. Zurbuchen, B. J. Anderson, H. Korth, R. L. Jr. McNutt, et al. (2015a), First observations of Mercury's plasma mantle by MESSENGER, *Geophys. Res. Lett.*, 42, 9666–9675, doi:10.1002/2015GL065805.
- DiBraccio, Gina A., James A. Slavin, Suzanne M. Imber, Daniel J. Gershman, Jim M. Raines, Caitriona M. Jackman, Scott A. Boardsen, Brian J. Anderson, Haje Korth, Thomas H. Zurbuchen, Ralph L. McNutt Jr., Sean C. Solomon, MESSENGER observations of flux ropes in Mercury's magnetotail, *Planetary and Space Science*, Volume 115, September 2015b, Pages 77-89, ISSN 0032-0633, <http://dx.doi.org/10.1016/j.pss.2014.12.016>.
- Dungey, J. W. (1961), Interplanetary Magnetic Field and the Auroral Zones, *Physical Review Letters.*, 6., 47-48, doi:10.1103/PhysRevLett.6.47.
- Egedal, J., W. Daughton and A. Le (2012), Large-scale electron acceleration by parallel electric fields during magnetic reconnection, *Nature Physics* 8, 321-324, doi:10.1038/nphys2249



- Fu, Z. F., and L. C. Lee (1985), Simulation of multiple X-line reconnection at the dayside magnetopause, *Geophys. Res. Lett.*, 12(5), 291–294, doi:10.1029/GL012i005p00291.
- Gershman, D. J., T. H. Zurbuchen, L. A. Fisk, J. A. Gilbert, J. M. Raines, B. J. Anderson, C. W. Smith, H. Korth, and S. C. Solomon (2012), Solar wind alpha particles and heavy ions in the inner heliosphere observed with MESSENGER, *J. Geophys. Res.*, 117, A00M02, doi:10.1029/2012JA017829.
- Gershman, D. J., J. A. Slavin, J. M. Raines, T. H. Zurbuchen, B. J. Anderson, H. Korth, D. N. Baker, and S. C. Solomon (2013), Magnetic flux pileup and plasma depletion in Mercury's subsolar magnetosheath, *J. Geophys. Res. Space Physics*, 118, 7181–7199, doi:[10.1002/2013JA019244](https://doi.org/10.1002/2013JA019244).
- Gosling, J. T., M. F. Thomsen, S. J. Bame, R. C. Elphic, and C. T. Russell (1990), Plasma flow reversals at the dayside magnetopause and the origin of asymmetric polar cap convection, *J. Geophys. Res.*, 95(A6), 8073–8084, doi:10.1029/JA095iA06p08073.
- Hill, T. W., Dessler, A. J. and Wolf, R. A. (1976), Mercury and Mars: The role of ionospheric conductivity in the acceleration of magnetospheric particles. *Geophys. Res. Lett.*, 3: 429–432. doi:10.1029/GL003i008p00429
- Hones Jr., E. W., J. R. Asbridge, S. J. Bame, M. D. Montgomery, S. Singer, and S.-I. Akasofu (1972), Measurements of magnetotail plasma flow made with Vela 4B, *J. Geophys. Res.*, 77(28), 5503–5522, doi:10.1029/JA077i028p05503.
- Horowitz, J. L., and T. E. Moore (1997), Four contemporary issues concerning ionospheric plasma flow to the magnetosphere, *Space Sci. Rev.*, 80, 49-76.
- Huang, C.-S., Evidence of periodic (2–3 hour) near-tail magnetic reconnection and plasmoid formation: Geotail observations, *Geophys. Res. Lett.*, 29(24), 2189, doi:[10.1029/2002GL016162](https://doi.org/10.1029/2002GL016162), 2002.
- Huddleston, D. E., C. T. Russell, G. Le, and A. Szabo (1997), Magnetopause structure and the role of reconnection at the outer planets, *J. Geophys. Res.*, 102(A11), 24289–24302, doi:10.1029/97JA02416.
- Imber, S. M., J. A. Slavin, S. A. Boardsen, B. J. Anderson, H. Korth, R. L. McNutt Jr., and S. C. Solomon (2014), MESSENGER observations of large dayside flux transfer events: Do they drive Mercury's substorm cycle?, *J. Geophys. Res. Space Physics*, 119, 5613–5623, doi:10.1002/2014JA019884.

Jasinski, J. M., et al. (2014), Cusp observation at Saturn's high-latitude magnetosphere by the Cassini spacecraft, *Geophys. Res. Lett.*, 41, 1382–1388, doi:10.1002/2014GL059319.

Jasinski, J. M., J. A. Slavin, C. S. Arridge, G. Poh, X. Jia, N. Sergis, A. J. Coates, and J. H. Waite Jr. (2016), Flux transfer event observation at Saturn's dayside magnetopause by the Cassini spacecraft, *Geophys. Res. Lett.*, 43, doi:10.1002/2016GL069260.

**G. H. Jones,**

Jia, X., J. A. Slavin, T. I. Gombosi, L. K. S. Daldorff, G. Toth, and B. van der Holst (2015), Global MHD simulations of Mercury's magnetosphere with coupled planetary interior: Induction effect of the planetary conducting core on the global interaction. *J. Geophys. Res. Space Physics*, 120, 4763–4775. doi: 10.1002/2015JA021143.

Johnson, C. L., et al. (2012), MESSENGER observations of Mercury's magnetic field structure, *J. Geophys. Res.*, 117, E00L14, doi:10.1029/2012JE004217.

Kivelson, M. G., and A. J. Ridley (2008), Saturation of the polar cap potential: Inference from Alfvén wing arguments, *J. Geophys. Res.*, 113, A05214, doi:10.1029/2007JA012302.

Knetter, T., F. M. Neubauer, T. Horbury, and A. Balogh (2004), Four-point discontinuity observations using Cluster magnetic field data: A statistical survey, *J. Geophys. Res.*, 109, A06102, doi:10.1029/2003JA010099.

Korth, H., B. J. Anderson, D. J. Gershman, J. M. Raines, J. A. Slavin, T. H. Zurbuchen, S. C. Solomon, and R. L. McNutt Jr. (2014), Plasma distribution in Mercury's magnetosphere derived from MESSENGER Magnetometer and Fast Imaging Plasma Spectrometer observations, *J. Geophys. Res. Space Physics*, 119, 2917–2932, doi:10.1002/2013JA019567.

Li, X., F. Guo, H. Li, and G. Li (2017), Particle acceleration during magnetic reconnection in a low-beta plasma, *The Astrophysical Journal*, Volume 843, 1, doi: <https://doi.org/10.3847/1538-4357/aa745e>

Lockwood, M., and M. F. Smith (1994), Low and middle altitude cusp particle signatures for general magnetopause reconnection rate variations: 1. Theory, *J. Geophys. Res.*, 99(A5), 8531–8553, doi:10.1029/93JA03399.

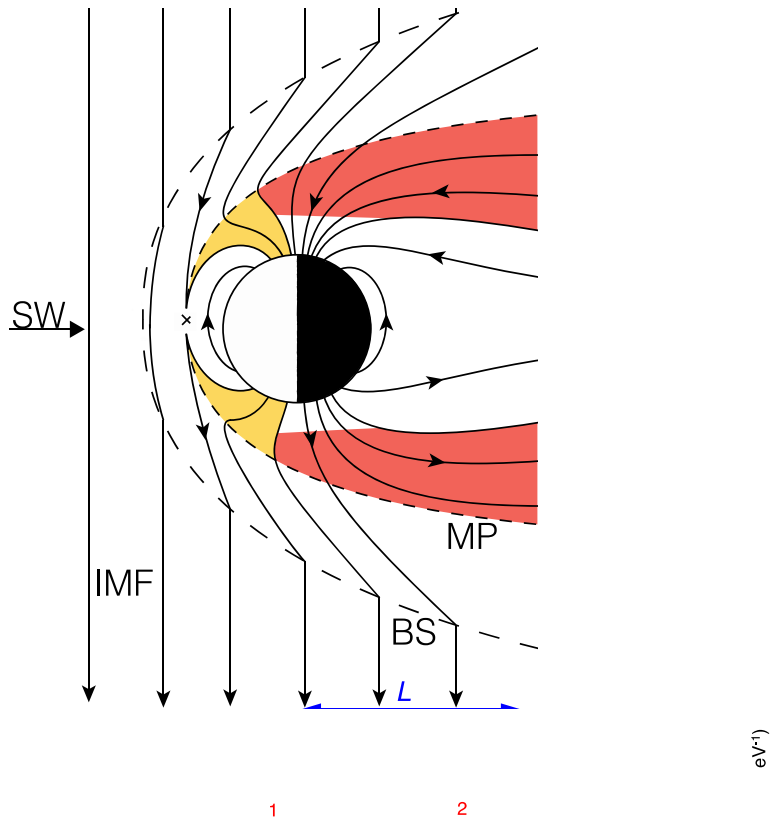
Mangano, V., S. Massetti, A. Milillo, C. Plainaki, S. Orsini, R. Rispoli, and F. Leblanc (2015), THEMIS Na exosphere observations of Mercury and their correlation with in-situ magnetic field measurements by MESSENGER, *Planet. Space Sci.*, 115, 102–109, doi:10.1016/j.pss.2015.04.001.

- Masters, A. (2014), Magnetic reconnection at Uranus' magnetopause, *J. Geophys. Res. Space Physics*, 119, 5520–5538, doi:10.1002/2014JA020077.
- Masters, A. (2015), Magnetic reconnection at Neptune's magnetopause, *J. Geophys. Res. Space Physics*, 120, 479–493, doi:10.1002/2014JA020744.
- Massetti, S., S. Orsini, A. Milillo and A. Mura (2007), Modelling Mercury's magnetosphere and plasma entry through the daysidemagnetosphere, *Planet. Space Sci.*, 55, 1557–1568, doi:10.1016/j.pss.2006.12.008.
- Massetti, S., V. Mangano, A. Milillo, A. Mura, S. Orsini, and C. Plainaki (2017), Short-term observations of double-peaked Na emission from Mercury's exosphere, *Geophys. Res. Lett.*, 44, 2970–2977, doi:10.1002/2017GL073090.
- Milan, S. E., G. Provan, and B. Hubert (2007), Magnetic flux transport in the Dungey cycle: A survey of dayside and nightside reconnection rates, *J. Geophys. Res.*, 112, A01209, doi:10.1029/2006JA011642.
- Pilipp, W. G., and G. Morfill (1978), The formation of the plasma sheet resulting from plasma mantle dynamics, *J. Geophys. Res.*, 83(A12), 5670–5678, doi:10.1029/JA083iA12p05670.
- Pitout, F., Escoubet, C. P., Klecker, B., and Rème, H.: Cluster survey of the mid-altitude cusp: 1. size, location, and dynamics, *Ann. Geophys.*, 24, 3011–3026, doi:10.5194/angeo-24-3011-2006, 2006.
- Poh, G., J. A. Slavin, X. Jia, J. M. Raines, S. M. Imber, W.-J. Sun, D. J. Gershman, G. A. DiBraccio, K. J. Genestreti, and A. W. Smith (2017), Mercury's cross-tail current sheet: Structure, X-line location and stress balance, *Geophys. Res. Lett.*, 44, 678–686, doi:10.1002/2016GL071612.
- Poh, G., *et al.* (2016), MESSENGER observations of cusp plasma filaments at Mercury, *J. Geophys. Res. Space Physics*, 121, 8260–8285, doi:[10.1002/2016JA022552](https://doi.org/10.1002/2016JA022552).
- Mozer, F. S., and A. Retin`o (2007), Quantitative estimates of magnetic field reconnection properties from electric and magnetic field measurements, *J. of Geophys. Res.*, 112, A10206, doi:10.1029/2007JA012406.
- Raines et al., (2011), MESSENGER observations of the plasma environment near Mercury, *Planet. Space Sci.*, 59, 2004–2015, doi:10.1016/j.pss.2011.02.004

- Raines, J. M., D. J. Gershman, J. A. Slavin, T. H. Zurbuchen, H. Korth, B. J. Anderson, and S. C. Solomon (2014), Structure and dynamics of Mercury's magnetospheric cusp: MESSENGER measurements of protons and planetary ions, *J. Geophys. Res. Space Physics*, 119, 6587–6602, doi:10.1002/2014JA020120.
- Ho, G., J.M Raines, Nguyen, L., Gannon, M., and Reid M., MESSENGER: Software Interface Specification for the Derived Records of the Energetic Particle and Plasma Spectrometer, NASA Planetary Data System, MESS-E\_V\_H\_SW-EPPS-3-FIPS-DDR-V2.0, 2016.
- Rassbach, M. E., R. A. Wolf, and R. E. Daniell Jr. (1974), Convection in a Martian magnetosphere, *J. Geophys. Res.*, 79(7), 1125–1127, doi:10.1029/JA079i007p01125.
- Reiff, P. H., T. W. Hill, and J. L. Burch (1977), Solar wind plasma injection at the dayside magnetospheric cusp, *J. Geophys. Res.*, 82(4), 479–491, doi:10.1029/JA082i004p00479.
- Rijnbeek, R. P., S. W. H. Cowley, D. J. Southwood, and C. T. Russell (1984), A survey of dayside flux transfer events observed by ISEE 1 and 2 magnetometers, *J. Geophys. Res.*, 89(A2), 786–800, doi:10.1029/JA089iA02p00786.
- Rosenbauer, H., H. Grünwaldt, M. D. Montgomery, G. Paschmann, and N. Sckopke (1975), Heos 2 plasma observations in the distant polar magnetosphere: The plasma mantle, *J. Geophys. Res.*, 80(19), 2723–2737, doi:10.1029/JA080i019p02723.
- Russell, C. T., and R. C. Elphic (1978), Initial ISEE magnetometer results—Magnetopause observations, *Space Sci. Rev.*, 22, 681–715, doi:10.1007/BF00212619.
- Russell, C. T., and R. C. Elphic (1979), ISEE observations of flux transfer events at the dayside magnetopause, *Geophys. Res. Lett.*, 6(1), 33–36, doi:10.1029/GL006i001p00033.
- Sanchez, E. R., and G. L. Siscoe (1990), IMP 8 magnetotail boundary crossings: A test of the MHD models for an open magnetosphere, *J. Geophys. Res.*, 95(A12), 20771–20779, doi:10.1029/JA095iA12p20771.
- Sarantos M., P. H. Reiff, T. W. Hill, R. M. Killen, A. L. Urquhart, A Bx-interconnected magnetosphere model for Mercury, *Planetary and Space Science*, Volume 49, Issues 14–15, December 2001, Pages 1629-1635, ISSN 0032-0633, [http://dx.doi.org/10.1016/S0032-0633\(01\)00100-3](http://dx.doi.org/10.1016/S0032-0633(01)00100-3).
- Siscoe, G. L., and E. Sanchez (1987), An MHD model for the complete open magnetotail boundary, *J. Geophys. Res.*, 92(A7), 7405–7412, doi:10.1029/JA092iA07p07405.

- Siscoe, G. L., N. F. Ness, and C. M. Yeates (1975), Substorms on Mercury?, *J. Geophys. Res.*, 80, 4359–4363, doi:10.1029/JA080i031p04359.
- Siscoe, G. L., N. U. Crooker, and K. D. Siebert, Transpolar potential saturation: Roles of region 1 current system and solar wind ram pressure, *J. Geophys. Res.*, 107(A10), 1321, doi:10.1029/2001JA009176, 2002a.
- Siscoe, G. L., G. M. Erickson, B. U. Ö. Sonnerup, N. C. Maynard, J. A. Schoendorf, K. D. Siebert, D. R. Weimer, W. W. White, and G. R. Wilson, Hill model of transpolar potential saturation: Comparisons with MHD simulations, *J. Geophys. Res.*, 107(A6), doi:10.1029/2001JA000109, 2002b.
- Sckopke N., H. Grunwaldt, M. .D. Montgomery, G. Paschmann, and H. Rosenbauer Observations of proton flow inside the high latitude magnetopause with the MPI plasma experiment on Heos 2, paper presented at Chapman Memorial Symposium on Magnetospheric Motions, AGU, Boulder, Colo., June 18-22, 1973.
- Sckopke, N., G. Paschmann, H. Rosenbauer, and D. H. Fairfield (1976), Influence of the interplanetary magnetic field on the occurrence and thickness of the plasma mantle, *J. Geophys. Res.*, 81(16), 2687–2691, doi:10.1029/JA081i016p02687.
- Sckopke N., Paschmann G., The plasma mantle. A survey of magnetotail boundary layer observations, *Journal of Atmospheric and Terrestrial Physics*, Volume 40, Issue 3, 1978, Pages 261-278, ISSN 0021-9169, [http://dx.doi.org/10.1016/0021-9169\(78\)90044-2](http://dx.doi.org/10.1016/0021-9169(78)90044-2).
- Shue, J.-H., J. K. Chao, H. C. Fu, C. T. Russell, P. Song, K. K. Khurana, and H. J. Singer (1997), A new functional form to study the solar wind control of the magnetopause size and shape, *J. Geophys. Res.*, 102(A5), 9497–9511, doi:10.1029/97JA00196.
- Slavin, J. A., E. J. Smith, D. G. Sibeck, D. N. Baker, R. D. Zwickl, and S.-I. Akasofu (1985), An ISEE 3 study of average and substorm conditions in the distant magnetotail, *J. Geophys. Res.*, 90(A11), 10875–10895, doi:10.1029/JA090iA11p10875.
- Slavin, J. A., Mercury's magnetosphere, *Advances in Space Research*, Volume 33, Issue 11, 2004, Pages 1859-1874, ISSN 0273-1177, <http://dx.doi.org/10.1016/j.asr.2003.02.019>.
- Slavin, J. A., et al. (2009), MESSENGER observations of magnetic reconnection in Mercury's magnetosphere, *Science*, 324, 606–610, doi:10.1126/Science.1172011.
- Slavin, J. A., et al. (2010), MESSENGER observations of extreme loading and unloading of Mercury's magnetic tail, *Science*, 329, 665–668, doi:10.1126/Science.1188067.

- Slavin, J. A., et al. (2012), MESSENGER observations of a flux-transfer-event shower at Mercury, *J. Geophys. Res.*, 117, A00M06, doi:10.1029/2012JA017926.
- Sonnerup, B. U., and L. J. Cahill Jr. (1967), Magnetopause structure and attitude from Explorer 12 observations, *J. Geophys. Res.*, 72(1), 171–183, doi:10.1029/JZ072i001p00171.
- Swisdak, M., B. N. Rogers, J. F. Drake, and M. A. Shay (2003), Diamagnetic suppression of component magnetic reconnection at the magnetopause, *J. Geophys. Res.*, 108, 1218, doi:10.1029/2002JA009726, A5.
- Tanskanen, E. I. (2009), A comprehensive high-throughput analysis of substorms observed by IMAGE magnetometer network: Years 1993–2003 examined, *J. Geophys. Res.*, 114, A05204, doi:[10.1029/2008JA013682](https://doi.org/10.1029/2008JA013682).
- Sun, W.-J., J. A. Slavin, S. Fu, J. M. Raines, Q.-G. Zong, S. M. Imber, Q. Shi, Z. Yao, G. Poh, D. J. Gershman, Z. Pu, T. Sundberg, B. J. Anderson, H. Korth, and D. N. Baker (2015), MESSENGER observations of magnetospheric substorm activity in Mercury's near magnetotail. *Geophys. Res. Lett.*, 42, 3692–3699. doi: 10.1002/2015GL064052.
- Sun, W. J., S. Y. Fu, J. A. Slavin, J. M. Raines, Q. G. Zong, G. K. Poh, and T. H. Zurbuchen (2016), Spatial distribution of Mercury's flux ropes and reconnection fronts: MESSENGER observations, *J. Geophys. Res. Space Physics*, 121, 7590–7607, doi:[10.1002/2016JA022787](https://doi.org/10.1002/2016JA022787).
- Sundberg, T., et al. (2012), MESSENGER observations of dipolarization events in Mercury's magnetotail, *J. Geophys. Res.*, 117, A00M03, doi:[10.1029/2012JA017756](https://doi.org/10.1029/2012JA017756).
- Winslow, R. M., B. J. Anderson, C. L. Johnson, J. A. Slavin, H. Korth, M. E. Purucker, D. N. Baker, and S. C. Solomon (2013), Mercury's magnetopause and bow shock from MESSENGER Magnetometer observations, *J. Geophys. Res. Space Physics*, 118, 2213–2227, doi:10.1002/jgra.50237.

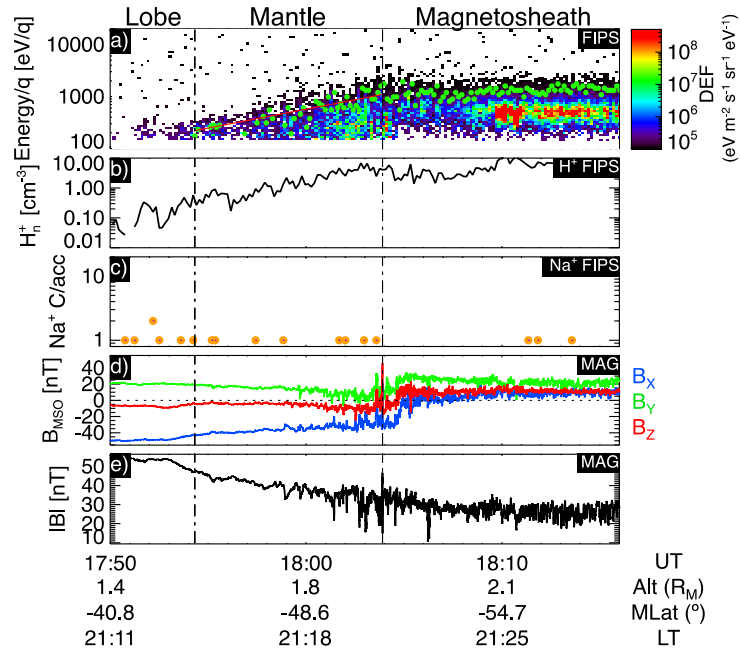


UT  
 Alt ( $R_M$ )  
 MLat ( $^\circ$ )  
 LT

**Above:**

**Figure 1.** An example of a MESSENGER trajectory on an average orbit in Mercury's magnetosphere and the associated observations. Top: a schematic of Mercury's magnetic field with the cusp (yellow shading) and mantle (red shading) highlighted and the corresponding trajectory of MESSENGER (shown in green). The directions of the drift velocity ( $V_{E \times B}$ ), parallel velocity ( $V_{\parallel}$ ) and the thickness  $d$  and length  $L$  are also shown. Bottom: a) FIPS proton counts

with the observed energy dispersions in the cusp (1) and mantle (2) underlined in red, (b) the three components of the observed magnetic field (MAG) in MSO coordinates, (c) magnitude of the magnetic field (MAG). The following acronyms are used: “SW” for solar wind, “M’sheath” for the magnetosheath, “IMF” for the interplanetary magnetic field, “BS” for the bow shock, “MP” for the magnetopause and ‘DEF’ for differential energy flux.



Author Manuscript



**Figure 2.** An example of a mantle observation on an outbound (anti-planetward) trajectory from the 10<sup>th</sup> of October 2011. The southern lobe and magnetosheath are observed before and after the plasma mantle, respectively. (a) FIPS ion energy spectrogram showing the differential energy flux (DEF). The green dots represent the lowest energy bin observed to have a signal to noise ratio of  $\geq 2.0$ , and a fit to these energies is shown in red to highlight the energy dispersion observed in the FIPS data. (b) FIPS calculated proton density moment, (c) FIPS Sodium counts per accumulation, (d) three components of the magnetic field observed by MAG and (e) magnetic field magnitude (MAG).

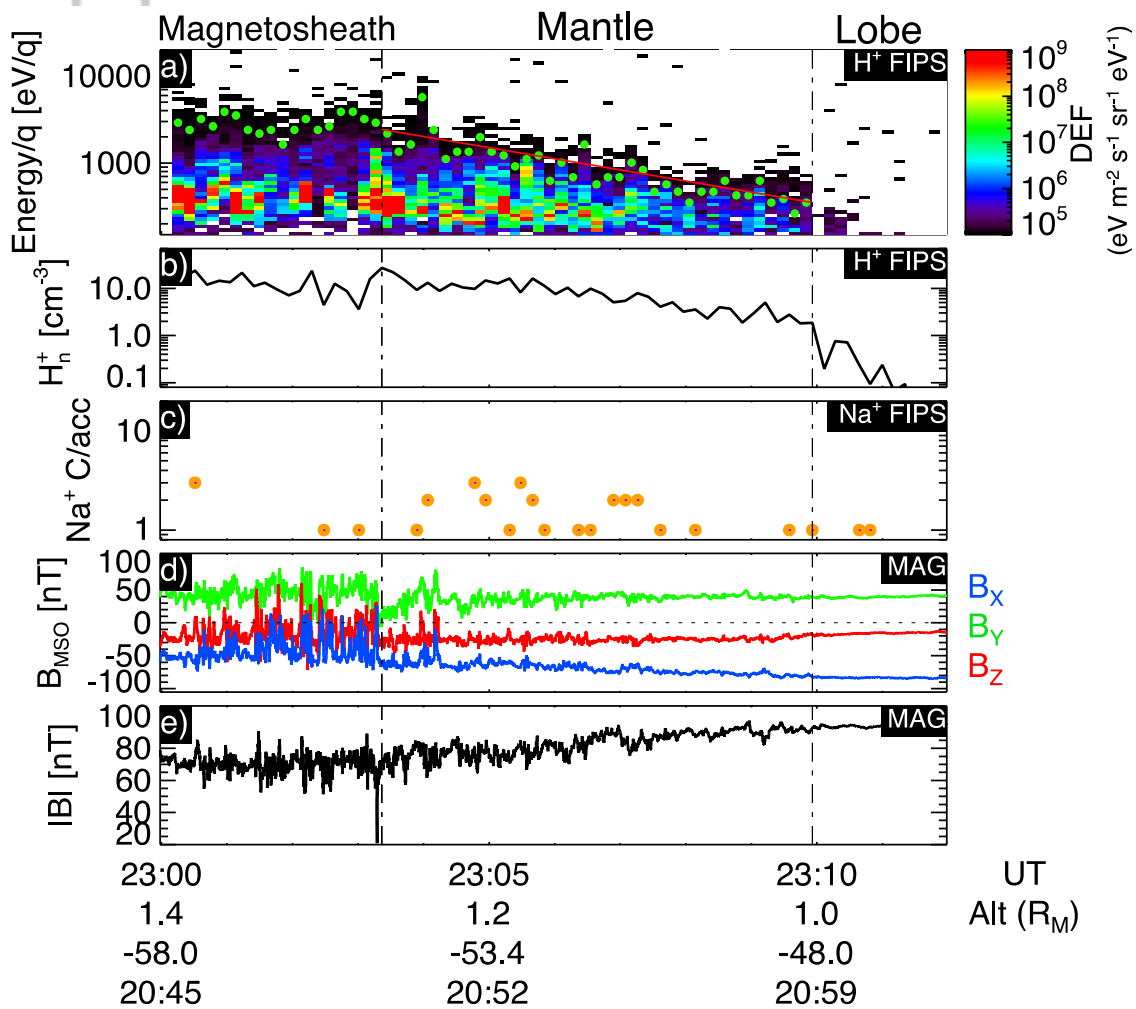
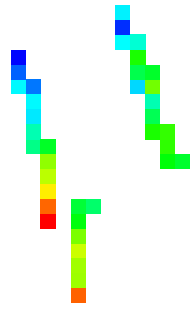


**Figure 3.** An example of a mantle observation on an inbound trajectory (planetward and equatorward) from the 10<sup>th</sup> of April 2015. The order in which the regions are observed is opposite to Figure 2, with the magnetosheath observed before and the lobe after the mantle. The format is the same as Figure 2.

Author Manuscript

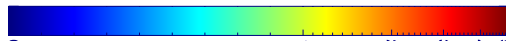
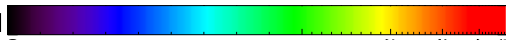
a)

b)



c)

Density [ $\text{cm}^{-3}$ ]



A

**Figure 4.** The average proton (a-c) and sodium (d-f) density maps of the observed plasma mantle events by the MESSENGER FIPS instrument. The locations are shown in aberrated Mercury-Solar-Orbital (MSO) coordinates where  $X'$  points from Mercury's center towards the oncoming solar wind,  $Z'$  is perpendicular to the orbital plane pointing northward, and  $Y'$  completes the right hand set. The panels on the left (a and d) are a view from dusk ( $X'$ - $Z'$ ) with model magnetospheric field lines shown in grey obtained from the global magnetospheric MHD model of Mercury [Jia et al., 2015]. The panels on the right are projections of the  $X'$ - $Y'$  (right) and  $Y'$ - $Z'$  planes (left). A model magnetopause is calculated using the Shue et al., (1997) magnetopause formulation, with a superimposed dipole offset of  $0.196 R_M$  which has been found at Mercury [Anderson et al., 2011, 2012; Johnson et al., 2012].

Author Manuscript

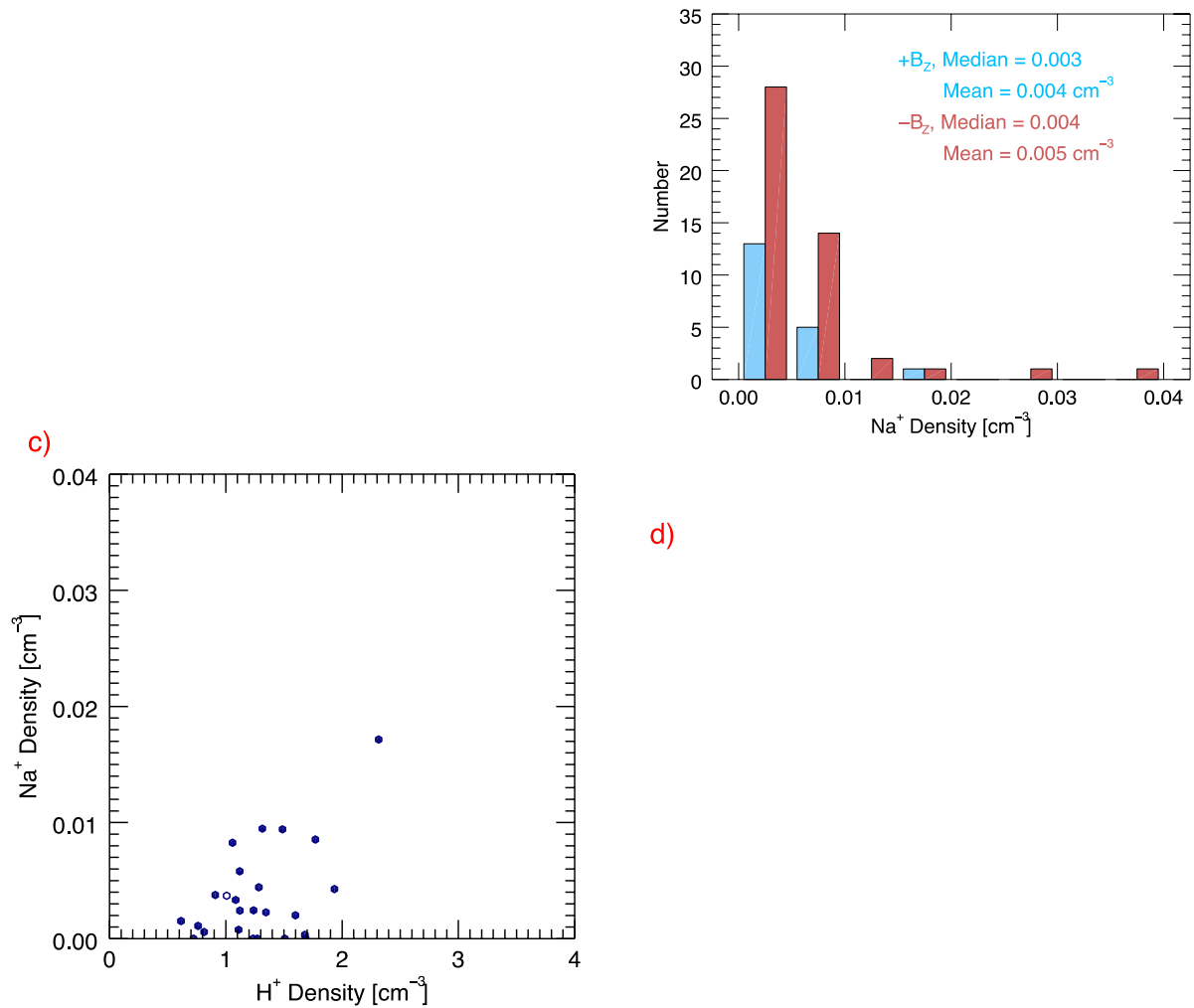


**Figure 5.** Histograms of the the averaged (over event) proton (a) and sodium (b) number density measurements. The densities are also divided into the estimated solar wind  $B_z$  orientation ( $-B_z$  is red,  $+B_z$  is blue). Panel c) shows the sodium to proton density relationship. Panel d) is a histogram of the cross-electric magnetospheric potential estimates.

Author

0 nT 0 nT

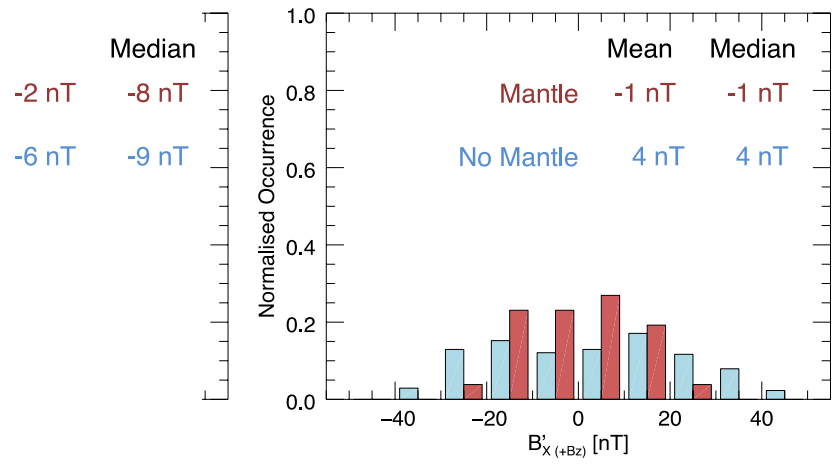


**Figure 6.** Results regarding the analysis of when we do not observe the plasma mantle. Panels a-b) show the trajectory of MESSENGER for five minutes inwards of the of the magnetopause in the X'-Y' and Y'-Z' planes, respectively (in aberrated MSO coordinates). Panels c-d) show histograms of the IMF magnitude and  $B_z$  conditions for when we see the mantle (red) and do not see the mantle (blue). Panels e-f) show the  $B_x$  component strength for -  $B_z$  and +  $B_z$  respectively.

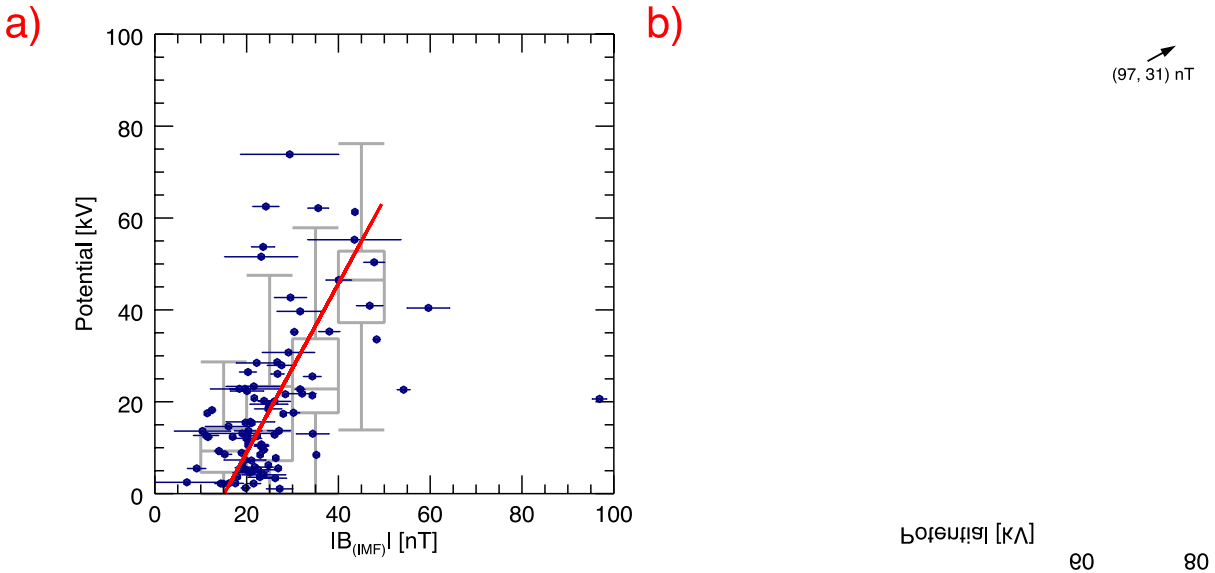


**Figure 7.** The plasma mantle potential estimates compared to the associated solar wind conditions: (a) the estimated cross-magnetospheric electric potential compared to the magnetic field magnitude of the IMF observed in the solar wind. The data is shown as box and whisker plots in grey, where the box represents the interquartile range (IQR), the central line shows the median and the whiskers length are 1.5 the IQR. These box plots were calculated for solar wind conditions in groups of 10 nT (0-9.9, 10-19.9 nT etc.). Panel b) shows the estimated potential dependence on both the IMF magnitude and the IMF  $B_z$ .

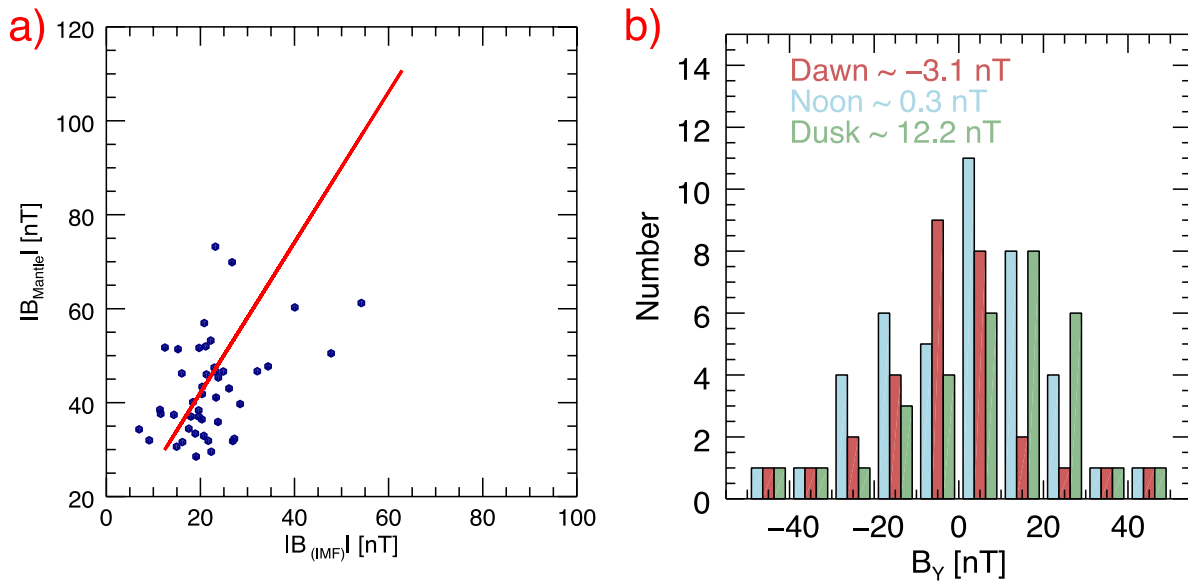


**Figure 8.** Panel a) shows the dependence of the observed mantle magnetic field strength on the IMF magnitude; (b) shows the location of the mantle observations compared to the  $B_Y$  orientation of the IMF. The mean IMF  $B_Y$  strength is shown at the top for each sector.

Author Manuscript